High-order harmonic signal of bond-length-variable C_{18} and its application in optical logic gates

Lihan Chi,[1] Yigeng Peng,[1,*] Chao Yu,[1,†] and Ruifeng Lu[1,2,‡]

[1]*Institute of Ultrafast Optical Physics, Department of Applied Physics and MIIT Key Laboratory of Semiconductor Microstructure and Quantum Sensing, Nanjing University of Science and Technology, Nanjing 210094, People's Republic of China*

[2]*State Key Laboratory of Molecular Reaction Dynamics, Dalian Institute of Chemical Physics, Chinese Academy of Sciences, Dalian 116023, People's Republic of China*

(Received 28 November 2023; accepted 30 January 2024; published 22 February 2024)

Recently, a solid-state-like high-harmonic generation (HHG) mechanism has been proposed from rotationally periodic molecules. Based on the *quasi*-energy band model, we investigate the HHG of ring-type polyynic cyclo[18]carbon (C_{18}) by further considering its bond length difference (R_{diff}) between the short and long C-C bonds. For R_{diff} values ranging from 0.06 to 0.12 Å with a linearly polarized laser, the seventh harmonic intensity of polyynic C_{18} exhibits the most significant structural sensitivity compared to the third and fifth harmonics. Transition energy level distribution, paired with time-frequency analysis and transition dipole moment behavior, indicate that the seventh harmonic arises from pure interband processes. Conversely, the HHG properties driven by two consecutive circularly polarized laser pulses at each considered laser intensity combination remain unaffected by changing these R_{diff} values. This characteristic allows polyynic C_{18} to be utilized for designing a variety of logic gate operations based on its harmonic ellipticity in ultrafast strong laser fields.

DOI: 10.1103/PhysRevA.109.023526

I. INTRODUCTION

Carbon, a ubiquitous nonmetallic element, is found extensively in both the atmosphere and the Earth's crust in a multitude of forms. Over the past 50 years, a myriad of novel carbon allotropes such as graphene [1], fullerene [2], and carbon nanotube [3] have garnered a lot of attention. It is fair to state that these novel carbon allotropes have been instrumental in driving advancements in chemistry and materials science, thanks to their unique properties and exceptional practical applicability. Consequently, even today, carbon allotropes continue to be at the forefront of both experimental synthesis and theoretical research [4–9].

Recently, the carbon family has welcomed a new member, an all-carbon atomic ring comprising 18 *sp*-hybridized carbon atoms, referred to as cyclo[18]carbon (C_{18}) [Fig. 1(a)]. This remarkable accomplishment by Kaiser *et al.* [10,11] in the synthesis and characterization of C_{18} has immediately sparked a surge of interest, prompting widespread investigations [12–14]. Particularly in recent years, many theoretical studies revolving around C_{18} have been undertaken, exploring aspects such as aromaticity [15,16], tunneling effect [17], vibrational spectra [18], and more.

In their groundbreaking work, Kaiser *et al.* identified that C_{18} exhibits a polyynic structure with alternating short and long C-C bonds instead of the cumulenic structure with equivalent C-C bonds, characterized by scanning tunneling microscopy (STM)/atomic force microscopy (AFM) techniques [10]. Baryshnikov *et al.* subsequently employed a comprehensive series of electronic structure calculations on C_{18}, utilizing both density functional theory (DFT) and the complete active space self-consistent field (CASSCF) methodology [15]. The polyynic molecular structure of C_{18}, as determined by DFT calculations, depends on the selection of appropriate functionals and is consistent with the results from CASSCF calculations.

Although Baryshnikov *et al.* identified the polyynic structure of C_{18}, the calculated bond length difference between the long and short C-C bonds shows discrepancies by different computational methods, ranging from about 0.06 to 0.12 Å. So far, the imaging resolution of conventional STM/AFM is inadequate for discerning such small spatial differences. To our understanding, these subtle structural alterations (0.06 – 0.12 Å) are also elusive even with some advanced imaging techniques, e.g., the high-angle annular dark-field imaging technique (∼0.5 Å) [19,20], and the state-of-the-art electron ptychography (∼0.39 Å) [21].

Interestingly, the change in symmetry of cumulenic C_{18} (D_{18h}) to polyynic C_{18} (D_{9h}) with slight geometric variances can alter the wave function pronouncedly, thereby notably affecting its nonlinear optical properties. The high-order harmonic generation (HHG), a vibrant area of interest in ultrafast strong field physics, has significantly expanded optical and spectroscopic approaches for exploring electronic structures as well as the dynamics of matter, which not only provides an effective means to achieve attosecond light sources, but also reveals more detailed structural information of the molecular and material systems. Therefore, the determination of structural information could potentially aid in assessing theoretical calculation strategies, such as functional selection. On the one hand, our earlier work confirmed the solid-state-like

*peng_yg@njust.edu.cn
†chaoyu@njust.edu.cn
‡rflu@njust.edu.cn

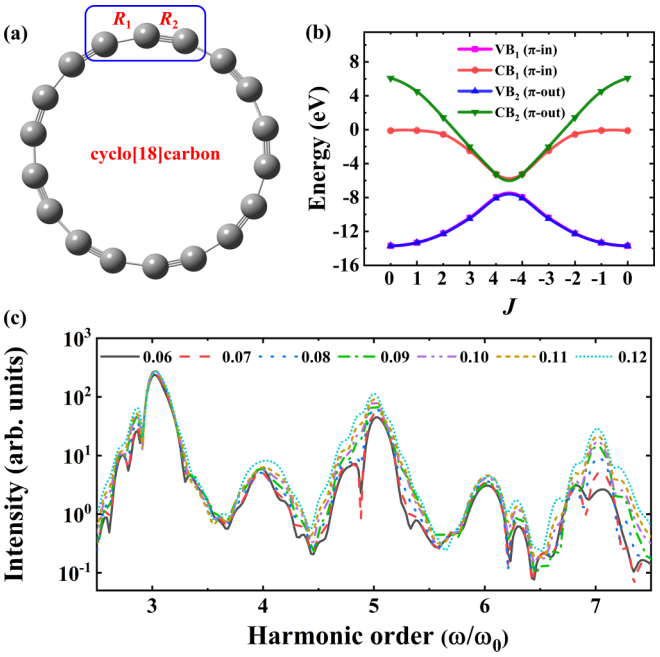

FIG. 1. (a) The structure of C_{18}. Note that C_{18} is an all-carbon atomic ring and it belongs to the D_{9h} point group. (b) The quasi-energy band structure of C_{18} with the R_{diff} of 0.12 Å in the framework of a generalized Bloch theorem with rotational invariance. Here, the four bands are abbreviated as VB_1, CB_1, VB_2, and CB_2. (c) Simulated harmonic spectrum of C_{18} based on the quasi-energy band model including π-in and π-out bands.

HHG of C_{18} and proposed its odd-even property as an all-optical method to address the symmetry puzzles [cumulence to polyyne (D_{18h} vs (D_{9h}))] about C_{18}. On the other hand, based on laser-driven quantum rings, the applications of HHG in logic gates have attracted interest [22,23]. Boolakee *et al.* measured the current response for different carrier envelope phases to realize light-field control of real and virtual charge carriers, bring petahertz logic gates processing closer to reality [24]. It is believed that logic gate operations utilizing ultrafast laser technology may play a pivotal role in optical communication, data processing, and enhancing the speed of computer operation.

In this paper, we further study the HHG characteristics of bond-length-variable C_{18} and seek its potential application in optical logic gates. Here, we define a parameter $R_{\text{diff}} = R_1 - R_2$ for the bond length difference between the long (R_1) and short (R_2) C-C bonds of C_{18}, as shown in Fig. 1(a). Our simulated results indicate that the HHG driven by linearly polarized lasers shows a notable structural sensitivity of polyynic C_{18}. This R_{diff}-dependent HHG appears to be more remarkably modulated by an interband process than by an intraband process. Moreover, the HHG characteristics of polyynic C_{18} driven by two consecutive circularly polarized laser pulses are almost unaffected in the considered R_{diff} values range. Extending from this observation, we hold the promise for multiple logic gate operations by harnessing the ellipticity of high-order harmonics of polyynic C_{18}.

II. COMPUTATIONAL DETAILS

We perform the HHG simulation at seven R_{diff} values (0.06, 0.07, 0.08, 0.09, 0.10, 0.11, 0.12 Å) of C_{18}. Since the STM and AFM measurements have accurately determined the radius of C_{18}, the radius and the C-C-C bond angle of C_{18} are fixed at 3.7 Å and 160 °, respectively.

As established in our previous work [25], for N-fold rotationally periodic systems, their eigenfunctions satisfy a generalized Bloch theorem [26–28],

$$\psi_J(\theta + \theta_0) = \psi_J(\theta) e^{iJ\theta_0}, \tag{1}$$

where $\theta_0 = 2\pi/N$ represents the rotation angle and J is angular momentum. According to the boundary condition $\psi_J(\theta + 2\pi) = \psi_J(\theta)$, J should be an integer, and $\psi_J = \psi_{J+N}$. It is obvious that $N = 9$ and $\theta_0 = 40^\circ$ for the polyynic C_{18} with the (D_{9h}) symmetry. On this basis, the values of J are from -4 to 4. Then a *quasi*-energy band structure of C_{18} can be obtained by combining the eigenenergies of all J. It is important to point out that C_{18} has two sets of 18-centered delocalized π electrons [29,30] (labeled π-in and π-out, respectively), of which 18 are occupied molecular orbitals (MOs) and 18 are unoccupied MOs. According to their energies and corresponding J values, the 36 π-in and π-out MOs are divided into four quasi-energy bands, as exhibited in Fig. 1(b) for $R_{\text{diff}} = 0.12$ Å. Herein, the occupied band can be viewed as the quasi-valence band (quasi-VB) and the unoccupied one as the quasi-conduction band (quasi-CB). Therefore, the four bands are labeled as quasi-VB_1, quasi-CB_1, quasi-VB_2, and quasi-CB_2, in which the π-in bands are subscribed by 1 and the π-out bands are subscribed by 2.

The calculations of the energy and wave function of C_{18} are carried out using the GAUSSIAN16 program packages [31] with the M06-2X [32] functional and 6-311++G(d,p) [33–35] basis set. Because the bound-state wave functions of the C_{18} molecule obtained by quantum chemistry calculations are real, a linear transformation [36] ($\psi_{\pm J} = \phi_J^a \pm i\phi_J^b$) is required to satisfy Eq. (1), where ϕ_J^a and ϕ_J^b represent a pair of degenerated π-in (or π-out) MOs.

By numerically solving the time-dependent Liouville–von Neumann equation, we can study the interaction between C_{18} and the external laser field,

$$i\frac{\partial \rho}{\partial t} = [H, \rho] - \frac{\rho^d - \rho_0^d}{T_1} - \frac{\rho - \rho^d}{T_2}, \tag{2}$$

where ρ is the density matrix, ρ^d and ρ_0^d are the diagonal terms of ρ and the initial density matrix ρ_0, respectively. The Hamiltonian matrix $H = U_n^J + \vec{E}(t) \cdot \vec{D}_{nn'}^{JJ'}$, consists of the diagonal term of quasi-energy band U_n^J and the nondiagonal term of the transition dipole moment (TDM) $\vec{D}_{nn'}^{JJ'} = \langle \psi_{nJ} | \vec{r} | \psi_{n'J'} \rangle$ where n/n' represents the band index. As is well known, the relaxation time T_1 of conventional semiconductors is about hundreds of femtoseconds or a few picoseconds and the dephasing time T_2 is usually assumed to a few femtoseconds (about half of an optical cycle) [37–39]. Here, we set T_1 and T_2 to 200 and 4 fs, respectively. In fact, we have evaluated the dephasing time in the range of 1–10 fs which indicates a slight influence on the simulated results of C_{18}. $\vec{E}(t)$ is

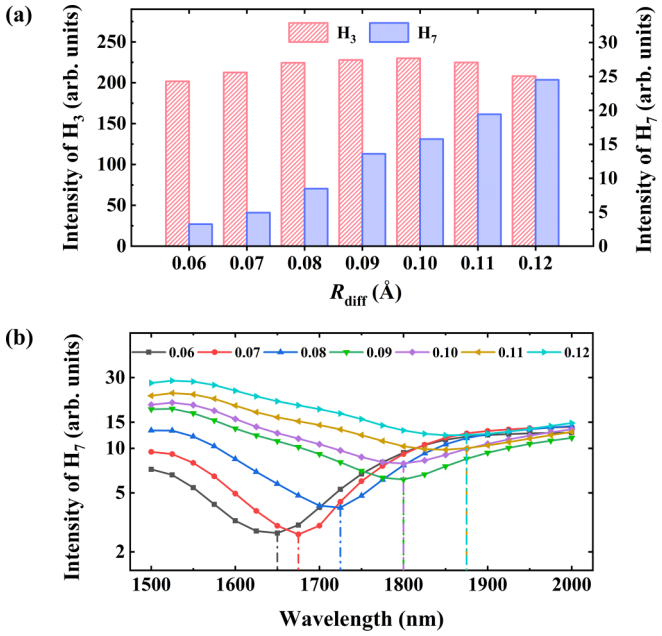

FIG. 2. (a) The intensities of the third (H_3) and seventh (H_7) harmonics of C_{18} at various R_{diff} values. The left axis corresponds to the intensity of H_3 and the right axis corresponds to the intensity of H_7. (b) The wavelength-dependent intensity of the seventh (H_7) harmonic on C_{18} at various R_{diff} values. The colored dashed lines indicate the locations of the H_7 minimum at various R_{diff} values.

the laser electric field, as shown at the bottom of Fig. 3(c). The time-dependent induced dipole $\vec{P}(t) = \text{Tr}[\rho(t)\vec{D}]$ can be calculated through the density matrix, then the HHG can be obtained from the Fourier transform of the dipole acceleration $\vec{a}(t) = \ddot{\vec{P}}(t)$. More computational details can be found in previous work [25].

III. RESULTS AND DISCUSSION

We first examine the R_{diff}-dependent HHG of C_{18} by considering the linearly polarized driving lasers. The polarization direction is fixed in the ring plane and the harmonic spectra are averaged at various directions. The laser wavelength of 1600 nm, the peak intensity of 1.0×10^{13} W/cm^2, and the full width at half maximum of the laser pulse of 45 fs are selected. Figure 1(c) depicts the simulated harmonic spectrum of C_{18} at various R_{diff} values. As the R_{diff} increases, the intensity of the third harmonic is basically unchanged, the intensity of the fifth harmonic exhibits a gradual increase, and the intensity of the seventh harmonic escalates much more notably. As plotted in Fig. 2(a), the intensity of the seventh harmonic (H_7) monotonically increases as a function of R_{diff}, while for comparison, the intensity of the third harmonic (H_3) is found basically unaffected by changing R_{diff}. This suggests that the seventh harmonic intensity could serve as a valuable metric for characterizing the subtle structural alteration of the polyynic C_{18} molecule. To corroborate the feasibility, we further investigate the wavelength-dependent behavior of the seventh harmonic intensity. From Fig. 2(b), distinct variation is observed by changing the incident laser wavelength. The intensity of the seventh harmonic changes dramatically when R_{diff} is small, and an obvious minimum at 1650 nm can be found when R_{diff} is 0.06 Å. However, when R_{diff} becomes larger than 0.09 Å, the wavelength-dependent behavior of the seventh harmonic intensity is reduced. We can also see that as R_{diff} increases, the minimum position of the seventh harmonic intensity moves in the direction of the long wavelength. Consequently, the seventh harmonic intensity properties under laser irradiation can be utilized as an optical method for reflecting the structural information of C_{18}.

To gain deeper insight into the structure-sensitive characteristics of the seventh harmonic intensity of C_{18}, we delve into the quasi-energy band structure, transition energy level distribution, time-frequency analysis, and TDM behavior. In fact, the quasi-energy bands of polyynic C_{18} display a very similar pattern for all considered R_{diff} values, i.e., a minor alteration in R_{diff} of C_{18} has a negligible impact on its quasi-energy band structure. Considering the quasi-energy band structures for seven R_{diff} values and according to the transition selection rule, we depict all the transition energy levels including intraband and interband processes in Fig. 3(a). It should be noted that the transition energy levels >6.5 eV are omitted, since these energies substantially exceed that of the seventh harmonic. As seen from Fig. 3(a), the interband transition energies for all considered R_{diff} values align with the energy interval corresponding to the seventh harmonic of fundamental laser wavelengths from 1550 to 2000 nm. By contrast, the intraband transition energies closely match the energy interval corresponding to the third harmonic. Hence, it is plausible to infer that the seventh and third harmonics originate dominantly from interband and intraband processes, respectively. In Fig. 3(b), we present a time-frequency analysis with R_{diff} of 0.12 Å to track the temporal evolution of harmonic intensity. It is evident that the seventh harmonic is produced separately for each optical cycle (o.c.) while the third harmonic is generated continuously. This substantiates the finding in Fig. 3(a) that the primary contributions to the seventh and third harmonics are attributed to the interband and intraband processes, respectively. It is worth noting that the signal strength around the center of the laser pulse shown in Fig. 3(b) is asymmetric. This phenomenon can be attributed to the depletion of the ground state. As depicted in Fig. 3(c), the time-dependent J-specific population of quasi-VB_1 oscillates obviously and becomes depleted (especially $J = \pm 4$) during the laser interaction. Furthermore, the intraband and interband TDMs for π-in bands of polyynic C_{18} with R_{diff} of 0.12 Å are plotted in Fig. 4. The calculated intraband TDM values nearby the diagonal squares are all close to 3.5 a.u. [Fig. 4(a)], which aligns with the half of the radius of C_{18} [25]. Nevertheless, the calculated interband TDM values [Fig. 4(b)] nearby the diagonal squares are notably smaller, ranging between 0.1 and 1 a.u. Compared with the intraband TDM values of 3.5 a.u., a notable increment in interband TDM values of C_{18} with the increasing of the R_{diff} value [Fig. 4(c)], reasonably explains the R_{diff}-independent third harmonic intensity and the R_{diff}-dependent seventh harmonic intensity. Moreover, TDM analysis can reasonably explain that the wavelength-dependent behavior of the seventh harmonic intensity seems to increase sharply [Fig. 2(b)] whereas the third harmonic intensity decreases linearly with the increasing of laser wavelength.

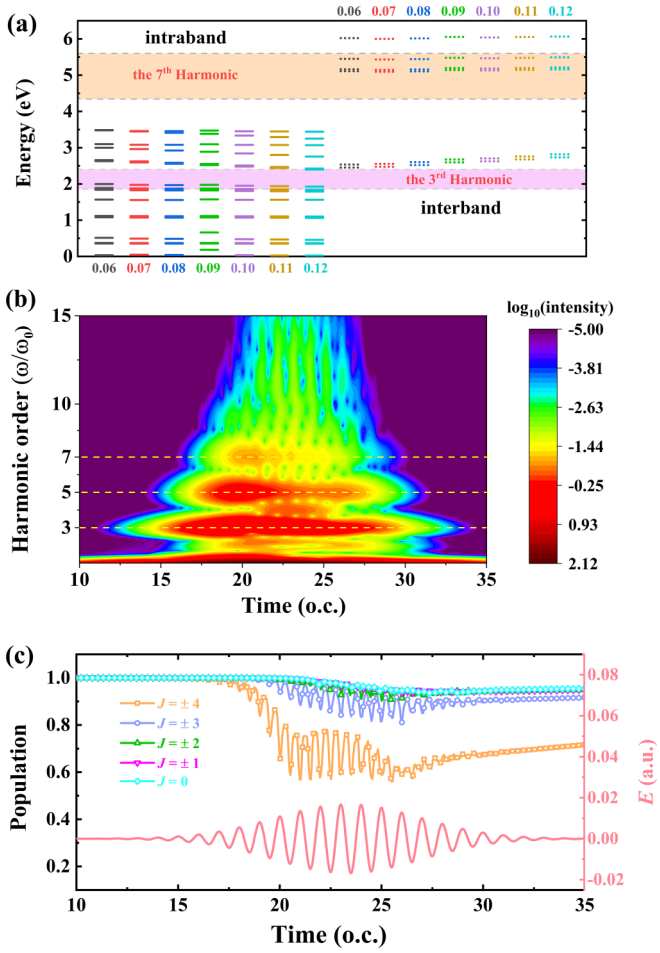

FIG. 3. (a) The transition energy level distribution of C_{18} at various R_{diff} values. The two types of transitions are identified as intraband (VB_1, CB_1, VB_2, CB_2) and interband ($VB_1 \leftrightarrow CB_1$, $VB_2 \leftrightarrow CB_2$). The lilac and orange areas indicate the energy ranges covered by the third and seventh harmonics, respectively. (b) The time-frequency analysis of C_{18} with the R_{diff} of 0.12 Å. The three dashed lines indicate the locations of the third, fifth, and seventh harmonics. Here, the photon energy (ω_0) of 0.775 eV and optical cycle (o.c.) of about 5.3 fs correspond to the laser wavelength of 1600 nm. (c) The time-dependent J-specific population of quasi-VB_1 of C_{18} with the R_{diff} of 0.12 Å. The light-red curve at the bottom indicates the waveform of the laser field. The left axis corresponds to the population of quasi-VB_1 of C_{18} and the right axis corresponds to the strength of the laser field.

Subsequently, we examine the HHG of polyynic C_{18} when subjected to circularly polarized lasers oriented in the ring plane. There have been several strict theoretical proofs [40–43] of the HHG selection rule for the N-fold system driven by a circularly polarized laser, and the $kN\pm1$ (the integer $k \geqslant 1$) harmonics are found. Such a selection rule is also valid in the polyynic C_{18} of ninefold symmetry. Therefore, it is easy to understand that the 10th, 19th, and 28th harmonics of polyynic C_{18} are right-handed with the same polarization of the incident light, while the 8th, 17th, and 26th harmonics are left-handed. We further study the HHG properties of polyynic C_{18} using two consecutive circularly polarized laser pulses with a time delay of 68 fs, of which the first is right-handed

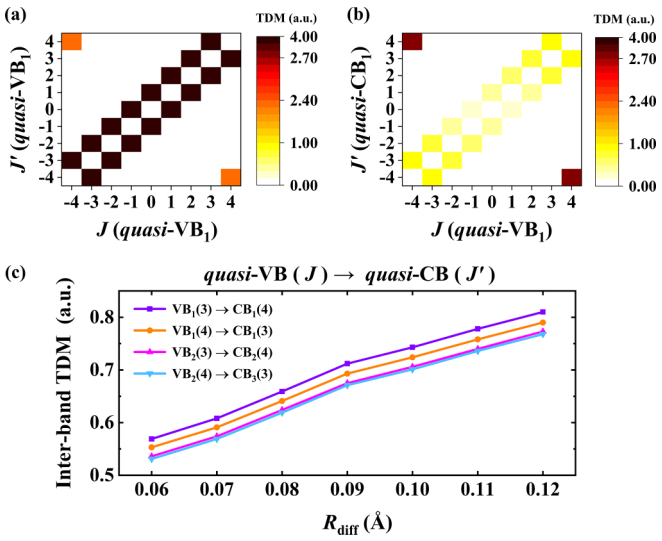

FIG. 4. (a) The intraband and (b) interband TDM values for π-in bands with the R_{diff} of 0.12 Å. Here, the absolute values of (a) intraband TDMs for quasi-VB_1 (the values for quasi-CB_1 are almost the same as quasi-VB_1) and (b) interband TDMs between quasi-VB_1 and quasi-CB_1 are shown. For π-out bands, the calculated intraband (between quasi-VB_2 and quasi-CB_2) and interband (between quasi-VB_2 and quasi-CB_2) TDM values with the R_{diff} of 0.12 Å are similar to π-in bands. (c) The interband TDM values involved in the seventh harmonic at various R_{diff} values of C_{18}. Here, the π-in bands are subscribed by 1 and π-out bands are subscribed by 2.

and the second is left-handed with the laser wavelength of 1600 nm and the full width at half maximum of 45 fs. Figure 5 shows the high-order harmonic spectra of C_{18} at $R_{\text{diff}} = 0.06$, 0.09, and 0.12 Å for the different laser intensity combinations of two circularly polarized lasers. From the top to the bottom of each laser intensity combination, it is evident that the harmonic characteristics of polyynic C_{18} maintain consistency regardless of R_{diff} values. This observation means that the HHG driven by two consecutive circularly polarized lasers does not depend on subtle structural alteration of polyynic C_{18}. For simplicity, our discussion and exploration of potential application focus on the HHG of C_{18} at $R_{\text{diff}} = 0.12$ Å.

In earlier studies, the application of HHG from ring model systems in logic gates was explored [22,23]. Our current research advances this concept to a realistic molecule, utilizing the unique HHG characteristics of polyynic C_{18}. Herein, we prompt the proposition of using the intensity of two driving laser pulses (I_1 and I_2) as logic input signals and the harmonic ellipticity of different orders as logic output signals. Specifically, the driving laser intensity of 1×10^{12} W/cm^2 is defined as input 0 and 1×10^{13} W/cm^2 is defined as input 1, i.e., $I_1 = 1 \times 10^{12}$ W/cm^2 and $I_1 = 1 \times 10^{13}$ W/cm^2 correspond to logic input (0,1). Then, the four logic inputs (0,0), (0,1), (1,0), and (1,1) can be obtained by considering the distinct intensity combinations of two laser pulses. Analogously, the harmonic ellipticity of polyynic C_{18} lower (higher) than the threshold value 0.5 is defined as output 0 (1).

Hereafter, we consider only the harmonic orders of polyynic C_{18} with higher intensity prior to the occurrence of the first main peak position ($k = 1$, the eighth and tenth

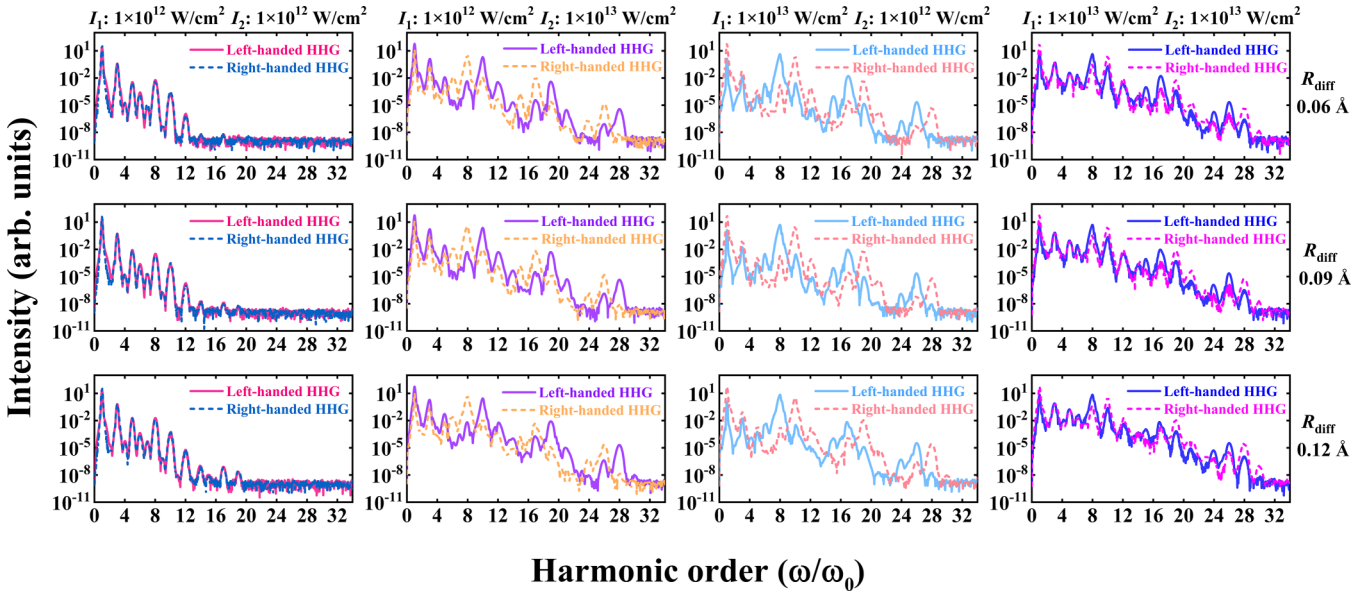

FIG. 5. Simulated harmonic spectra of C_{18} driven by two consecutive circularly polarized laser pulses across various R_{diff} values. Each row shares the same R_{diff} value, while each column shares the same intensity combination.

harmonics). Based on HHG characteristics of polyynic C_{18}, we demonstrate the feasibility of constructing optical logic gates using the ellipticity values of the third (H_3), fifth (H_5), sixth (H_6), eighth (H_8), and tenth (H_{10}) harmonics under four distinct logic inputs. The construction of XOR and OR logic gates and the corresponding truth tables are provided in Figs. 6(a) and 6(b). We can see that the ellipticity values of all considered harmonics (H_3, H_5, H_6, H_8, and H_{10}) output 1 in the presence of inputs (0,1) and (1,0), while output 0 in the presence of input (0,0). With the input (1,1), the ellipticity values of the third, fifth, and sicth harmonics output 0, while the ellipticity values of the eighth and tenth harmonics output 1. What is more, by inverting the assignment of the logical input and output, the H_8 and H_{10} signals can be utilized to construct logic AND gates operations. When the threshold of harmonic ellipticity is set to 0.8, the RESET gate can be achieved by using the H_3 and H_5 signals, the XOR gate can be obtained by the H_6 signal, and the OR gate can be still achieved by the H_8 and H_{10} signals. Moreover, these elementary logic gates can be obtained by considering a broader set of laser intensity combination and threshold value of harmonic ellipticity. Finally, we also examine the harmonic spectra of cumulenic C_{18} driven by two consecutive circularly polarized laser pulses. However, the spectral peaks we are concerned about are flooded in many cases. Consequently, it is difficult to realize the logic gate operations based on the HHG properties of cumulenic C_{18} by exploring various laser intensity combinations.

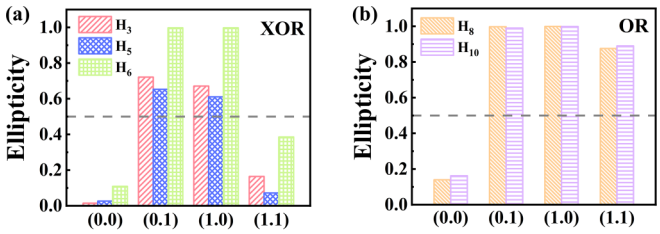

Input		Output
0	0	0
0	1	1
1	0	1
1	1	0

Input		Output
0	0	0
0	1	1
1	0	1
1	1	1

FIG. 6. The designed XOR (a) and OR (b) optical logic gates and the corresponding truth tables.

IV. CONCLUSION

In summary, on the basis of the quasi-energy band model proposed in our previous work, we simulate the HHG of C_{18} at various R_{diff} values. Our results indicate the sensitive dependence of the seventh harmonic intensity on R_{diff} of C_{18} in linearly polarized laser fields. The wavelength-dependent behavior of the seventh harmonic intensity is further suggested to optically discern subtle structural alterations of polyynic C_{18}, which potentially outperforms traditional imaging techniques. The transition energy level distribution and the time-frequency analysis find that the seventh harmonic predominantly stems from interband processes, while the TDM behavior properly explains the interband and intraband processes of HHG. More interestingly, when we fix the laser intensity combination of two consecutive circularly polarized laser pulses, the properties of the radiated HHG are hardly influenced by subtle structural alterations of polyynic C_{18}. By modulating the intensity combinations of the two delayed laser pulses as the logic input signals and the harmonic ellipticity as the logic output signals, a variety of elementary logic gates (XOR, OR, AND, RESET) can be designed. The realization of multiple logic gate operations supported by ultrafast laser technology will provide more possibilities for fundamental discoveries and prospective technological applications in the future.

ACKNOWLEDGMENTS

This work was supported by the National Key Research and Development Program of China (Grant No. 2022YFA1604301), the NNSF of China (Grants No. 11974185, No. 11904028, No. 12174195, No. 11834004, and No. 12374237), and the Natural Science Foundation of Jiangsu Province (Grant No. BK20170032).

[1] H. W. Kroto, J. R. Heath, S. C. O'Brien, R. F. Curl, and R. E. Smalley, C_{60}: Buckminsterfullerene, Nature (London) **318**, 162 (1985).

[2] S. Iijima and T. Ichihashi, Single-shell carbon nanotubes of 1-nm diameter, Nature (London) **363**, 603 (1993).

[3] K. S. Novoselov, A. K. Geim, S. V. Morozov, D. Jiang, Y. Zhang, S. V. Dubonos, I. V. Grigorieva, and A. A. Firsov, Electric field effect in atomically thin carbon films, Science **306**, 666 (2004).

[4] B. G. Kim and H. J. Choi, Graphyne: Hexagonal network of carbon with versatile Dirac cones, Phys. Rev. B **86**, 115435 (2012).

[5] G. Povie, Y. Segawa, T. Nishihara, Y. Miyauchi, and K. Itami, Synthesis of a carbon nanobelt, Science **356**, 172 (2017).

[6] T. Wei, F. Hauke, and H. Andreas, Covalent inter-synthetic-carbon-allotrope hybrids, Acc. Chem. Res. **52**, 2037 (2019).

[7] M. D. Kilde, A. H. Murray, C. L. Andersen, F. E. Storm, K. Schmidt, A. Kadziola, K. V. Mikkelsen, F. Hampel, O. Hammerich, R. R. Tykwinski *et al.*, Synthesis of radiaannulene oligomers to model the elusive carbon allotrope 6,6,12-graphyne, Nat. Commun. **10**, 3714 (2019).

[8] Z. Zuo, D. Wang, J. Zhang, F. Lu, and Y. Li, Synthesis and applications of graphdiyne-based metal-free catalysts, Adv. Mater. **31**, 1803762 (2019).

[9] C. H. Shu, M. X. Liu, Z. Q. Zha, J. L. Pan, S. Z. Zhang, Y. L. Xie, J. L. Chen, D. W. Yuan, X. H. Qiu, and P. N. Liu, On-surface synthesis of poly (*p*-phenylene ethynylene) molecular wires via in situ formation of carbon-carbon triple bond, Nat. Commun. **9**, 2322 (2018).

[10] K. Kaiser, L. M. Scriven, F. Schulz, P. Gawel, L. Gross, and H. L. Anderson, An sp-hybridized molecular carbon allotrope, cyclo[18]carbon, Science **365**, 1299 (2019).

[11] L. M. Scriven, K. Kaiser, F. Schulz, A. J. Sterling, S. L.Woltering, P. Gawel, K. E. Christensen, H. L. Anderson, and L. Gross, Synthesis of cyclo[18]carbon via debromination of $C_{18}Br_6$, J. Am. Chem. Soc. **142**, 12921 (2020).

[12] Z. Liu, T. Lu, and Q. Chen, An sp-hybridized all-carboatomic ring, cyclo[18]carbon: Electronic structure, electronic spectrum, and optical nonlinearity, Carbon **165**, 461 (2020).

[13] A. J. Stasyuk, O. A. Stasyuk, M. Sola, and A. A. Voityuk, Cyclo[18]carbon: The smallest all-carbon electron acceptor, Chem. Commun. **56**, 352 (2020).

[14] L. Zhang, H. Li, Y. P. Feng, and L. Shen, Diverse transport behaviors in cyclo[18]carbon-based molecular devices, J. Phys. Chem. Lett. **11**, 2611 (2020).

[15] G. V. Baryshnikov, R. R. Valiev, A. V. Kuklin, D. Sundholm, and H. Agren, Cyclo[18]carbon: Insight into electronic structure, aromaticity, and surface coupling, J. Phys. Chem. Lett. **10**, 6701 (2019).

[16] Z. Liu, T. Lu, and Q. Chen, An sp-hybridized all-carboatomic ring, cyclo[18]carbon: Bonding character, electron delocalization, and aromaticity, Carbon **165**, 468 (2020).

[17] A. Nandi, E. Solel, and S. Kozuch, Carbon tunneling in the automerization of cyclo[18]carbon, Chem. Eur. J. **26**, 625 (2020).

[18] Z. Liu, T. Lu, and Q. Chen, Vibrational spectra and molecular vibrational behaviors of all-carboatomic rings, cyclo[18]carbon and its analogues, Chem. Asian J. **16**, 56 (2021).

[19] H. Sawada, Y. Tanishiro, N. Ohashi, T. Tomita, F. Hosokawa, T. Kaneyama, Y. Kondo, and K. Takayanagi, STEM imaging of 47-pm-separated atomic columns by a spherical aberration-corrected electron microscope with a 300-kV cold field emission gun, J. Microsc. **58**, 357 (2009).

[20] R. Erni, M. D. Rossell, C. Kisielowski, and U. Dahmen, Atomic-resolution imaging with a sub-50-pm electron probe, Phys. Rev. Lett. **102**, 096101 (2009).

[21] Y. Jiang, Z. Chen, Y. Han, P. Deb, H. Gao, S. Xie, P. Purohit, M. W. Tate, J. Park, S. M. Gruner *et al.*, Electron ptychography of 2D materials to deep sub-angstrom resolution, Nature (London) **559**, 343 (2018).

[22] D. Cricchio and E. Fiordilino, Laser driven quantum rings: One byte logic gate implementation, RSC Adv. **8**, 3493 (2018).

[23] D. Cricchio and E. Fiordilino, Wavelet analysis and HHG in nanorings: Their applications in logic gates and memory mass devices, Nanoscale **8**, 1968 (2016).

[24] T. Boolakee, C. Heide, A. Garzón-Ramírez, H. B. Weber, I. Franco, and P. Hommelhoff, Light-field control of real and virtual charge carriers, Nature (London) **605**, 251 (2022).

[25] Y. Peng, T. Wu, G. Yuan, L. Chi, S. Jiang, K. Dorfman, C. Yu, and R. Lu, Solid state–like high harmonic generation from cluster molecules with rotational periodicities, Sci. Adv **9**, eadd6810 (2023).

[26] E. Dobardžić, M. Dimitrijević, and M. V. Milovanović, Generalized Bloch theorem and topological characterization, Phys. Rev. B **91**, 125424 (2015).

[27] O. O. Kit, L. Pastewka, and P. Koskinen, Revised periodic boundary conditions: Fundamentals, electrostatics, and the tight-binding approximation, Phys. Rev. B **84**, 155431 (2011).

[28] Y. C. Lee and W. Z. Lee, Rotational states of a benzenelike ring and Bloch's theorem, Am. J. Phys. **77**, 1144 (2009).

[29] P. W. Fowler, N. Mizoguchi, D. E. Bean, and R. W. A. Havenith, Double aromaticity and ring currents in all-carbon rings, Chem. Eur. J. **15**, 6964 (2009).

[30] F. Diederich, Y. Rubin, C. B. Knobler, R. L. Whetten, K. E. Schriver, K. N. Houk, and Y. Li, All-carbon molecules: Evidence for the generation of cyclo[18]carbon from a stable organic precursor, Science **245**, 1088 (1989).

[31] M. J. Frisch, G. W. Trucks, H. B. Schlegel, G. E. Scuseria, M. A. Robb, J. R. Cheeseman, G. Scalmani, V. Barone, G. A. Petersson, H. Nakatsuji *et al.*, *Gaussian16, Revision C.01* (Gaussian, Inc., Wallingford, CT, 2016).

[32] Y. Zhao and D. G. Truhlar, The M06 suite of density functionals for main group thermochemistry, thermochemical kinetics, noncovalent interactions, excited states, and transition elements: Two new functionals and systematic testing of four M06-class

functionals and 12 other functionals, Theor. Chem. Acc. **120**, 215 (2008).

[33] M. J. Frisch, J. A. Pople, and J. S. Binkley, Self-consistent molecular orbital methods 25. Supplementary functions for Gaussian basis sets, J. Chem. Phys. **80**, 3265 (1984).

[34] R. Krishnan, J. S. Binkley, R. Seeger, and J. A. Pople, Self-consistent molecular orbital methods. XX. A basis set for correlated wave functions, J. Chem. Phys. **72**, 650 (1980).

[35] T. Clark, J. Chandrasekhar, G. W. Spitznagel, and P. V. R. Schleyer, Efficient diffuse function augmented basis sets for anion calculations. III. The 3-21+G basis set for first-row elements, Li-F, J. Comput. Chem. **4**, 294 (1983).

[36] M. Kanno, Y. Ono, H. Kono, and Y. Fujimura, Laser-polarization effects on coherent vibronic excitation of molecules with quasi-degenerate electronic states, J. Phys. Chem. A **116**, 11260 (2012).

[37] S. V. Rao and D. N. Rao, Excited state dynamics of C_{60} studied using incoherent light, Chem. Phys. Lett. **283**, 227 (1998).

[38] S. K. Sundaram and E. Mazur, Inducing and probing non-thermal transitions in semiconductors using femtosecond laser pulses, Nat. Mater. **1**, 217 (2002).

[39] S. Y. Kruchinin, F. Krausz, and V. S. Yakovlev, *Colloquium*: Strong-field phenomena in periodic systems, Rev. Mod. Phys. **90**, 021002 (2018).

[40] F. Ceccherini, D. Bauer, and F. Cornolti, Dynamical symmetries and harmonic generation, J. Phys. B **34**, 5017 (2001).

[41] X. Liu, X. Zhu, L. Li, Y. Li, Q. Zhang, P. Lan, and P. Lu, Selection rules of high-order-harmonic generation: Symmetries of molecules and laser fields, Phys. Rev. A **94**, 033410 (2016).

[42] A. Fleischer, O. Kfir, T. Diskin, P. Sidorenko, and O. Cohen, Spin angular momentum and tunable polarization in high-harmonic generation, Nat. Photonics **8**, 543 (2014).

[43] O. E. Alon, V. Averbukh, and N. Moiseyev, Selection rules for the high harmonic generation spectra, Phys. Rev. Lett. **80**, 3743 (1998).